DOI: 10.13009/EUCASS2017-365

DOI: 365

Aerodynamic Design of a Martian Micro Air Vehicle

T.Désert, J-M.Moschetta and H.Bézard*
ONERA & ISAE-SUPAERO
2 Avenue Edouard Belin, 31000 Toulouse, France
thibault.desert@onera.fr · jean-marc.moschetta@isae.fr · herve.bezard@onera.fr
*Corresponding author

Abstract

The present study aims at developing a reliable propulsion system for a rotary wing micro air vehicle (MAV) associated to rovers in order to enhance Martian exploration rate. Since subsonic compressible ultra low Reynolds number ($2000 < Re_{dom} < 10\,000$) flows are unusual and unknown in the biosphere, an evaluation of numerical tools has been carried out recreating a depressurized experiment. 3D simulations by ONERA's laminar unsteady Navier-Stokes solver elsA successfully retrieve measured forces in cases of not fully detached flow on the airfoil. The unsteady solver is validated for ultra low Reynolds number and compared in 2D to steady computations using the solvers elsA and XFoil. Steady computations provide valuable hints on airfoil's performances anterior to heavy boundary layer separation. Therefore, based on XFoil's performances evaluations, camber line and thickness distribution have been optimized for 2D incompressible and compressible flow behavior apprehension. Optimal shape is a highly cambered airfoil shifting the boundary layer separation downstream. However, optimization process being steady, optimums cannot rely on vortex production enhancement, like corrugated airfoils. The impact of airfoil optimization and vortex production enhancement are estimated with 2D unsteady Navier-Stokes computations comparing the compressible optimized airfoil shape to airfoils picked from literature. The first conclusion is that airfoils delaying heavy unsteadiness generation are producing higher lift and lower drag in 2D than the airfoils enhancing vortex production we picked. Second conclusion is that among airfoils delaying boundary layer detachment, steady optimization process does not provide tromendous improvement in 2D aerodynamic performances. However, a minor 2D performances enhancement might have a greater magnitude on 3D flows. In order to evaluate the tendency in 3D, a automatized blade-element/vortex method rotor design process has been characterized. The process being based on 2D unsteady polars, the impact on 3D flows will be evaluated with an upcoming experimental campaign. The experimental facility is a ONERA's $18m^3$ tank recreating Martian atmosphere in terms on kinematic viscosity and composition. The tank size will allow to reduce wall effects and provide - as compared to previous studies - a more accurate evaluation of rotor performances.

1. Introduction

Since 2004, three exploration rovers have successfully landed on the Martian surface. Yet, only about sixty kilometers have been explored on 21 000 km of the planet's circumferential path. The slow exploration rate is mainly due to a lack of visibility on the ground. A rotary wing micro air vehicle (MAV) associated to rovers could significantly increase their mobility by providing an aerial point of view of their path. However, Martian atmosphere is far from MAV friendly: density is hundred times lower than on Earth and speed of sound is also lower due to low temperature and different atmosphere composition (96% of CO_2). Hence, a new aerodynamic domain is explored: compressible ultra low Reynolds number flows - table 1.

So far, the very few papers operating in our Reynolds number range are mostly studying the impact of Reynolds number[5] and turbulence rate[18,17] on flow laminarity or evaluating aerodynamic performances of typical airfoils[16] and planform distributions.[1] Only two studies provide airfoil camber line optimization at $Re_c = 6000$[11] and $Re_c = [6000, 16000]$[12] for incompressible flows. Neither thickness distribution nor compressible optimization have been undertaken yet. Incompressible experimental devices are usually low speed wind tunnels,[5] water tunnels[18,16] or nanorotors[11].[12] As far as we know, only two depressurized experiments recreate compressible ultra-low Reynolds number conditions for airfoil[13] or rotor[15] performances measurement. However, neither studies provide a validated computational tool for flow simulation. In the present study, a computational tool is validated on compressible ultra low

DOI: 10.13009/EUCASS2017-365

Table 1: Atmospheric conditions of Mars and the Earth at ground level

	Earth	**Mars**
Density (kg/m^3)	1.225	0.014
Dynamic viscosity (mPa.s)	0.0181	0.0106
Average temperature (°C)	15	-63
Speed of sound (m/s)	340	238

Reynolds number flows. Moreover, incompressible and compressible airfoil optimizations of both camber line and thickness distributions are carried out. The optimized airfoils are evaluated and compared to airfoils from literature with the validated solver.
This paper presents an aerodynamic design of a MAV operating in Martian atmosphere. First, MAV's flight conditions domain is defined. In this domain, steady and unsteady numerical tools are evaluated and compared to *Mars Wind Tunnel* experiment.[13] Then, a compressible airfoil shape optimization process based on 2D steady performances is characterized and carried out step by step for flow behavior apprehension. Finally, an automatized numerical process based on blade-element/vortex method is presented and different designs of rotors are built with liquid resin 3D printer for the upcoming experimental campaign.

2. Description of Martian Micro Air Vehicle flight conditions

Aerodynamic design's domain of the rotary wing MAV correspond to the MAV's flight conditions in hover: Reynolds Number and Mach number range. These two dimensionless quantities depend on atmospheric conditions, MAV's size, weight and rotational speed. The constraints are the diameter of the MAV being 30 cm, its weight about 200 g and the maximum rotational speed set to avoid locally supersonic flow.
2D laminar steady Navier-Stokes computations set maximal subsonic rotational speed to 12 000 rpm corresponding to $M = 0.8$ at blade's tip for $c = 238 m.s^{-1}$ ($T = -63°C$). Chord Reynolds number range is determined via BEMT evaluations with a number of blades range $n_{blades} \in [\![2, 5]\!]$: $2000 < Re_{dom} < 10\ 000$. The upper boundary of the Reynolds number range is enhanced in case of heavier MAV design. The reference Reynolds number is: $Re_{ref} = 3000$.

3. Assessment of 2D and 3D numerical tools for compressible ultra-Low Reynolds number flows

Numerical tools are not scaled on compressible ultra-Low Reynolds number flows. Solvers need to be evaluated and compared to an experiment recreating Martian atmospheric conditions : the *Mars Wind Tunnel*. The unsteady solver, elsA,[2] is validated on a 3D simulation recreating the test section and a steady quick solver, XFoil,[6] is assessed for the airfoil optimization process.

3.1 Tohoku's University *Mars Wind Tunnel* experiment[13]

The *Mars Wind Tunnel* (MWT) experimental device is located at Tohoku's University - figure 1(a). It consists of a wind tunnel reproducing Martian atmospheric composition: density and gas. We evaluated the case of the triangular airfoil[13] presented in figure 1(b). This airfoil's strong leading edge camber and sharpness causes significant unsteadiness in the flow, making it interesting for numerical validation. Low density allows to reach $Re_c = 3000$ for different Mach numbers - $M = 0.15$ & 0.5. Forces are mesured with a balance and pressure distributions are available on the upper part of the airfoil thanks to pressure sensitive paint (PSP). Even if the MWT experiment is supposed to recreate 2D flows, PSP measurement showed a three dimensionality over the airfoil. Moreover, author's 3D simulations[13] provide greater lift and drag predictions than the experiment while not taking into account the test sections - figure 2(b). This phenomenon is due to wall effect on the sides on the test section: the entire experiment needs to be simulated for proper flow and forces evaluations.

3.2 3D unsteady Navier-Stokes solver elsA

The solver elsA was developed by ONERA in the 90's. It is based on an integral form of the compressible Navier-Stokes equations.[2] Considering the Reynolds number range, the hypothesis of laminar flow in a non turbulent environment

DOI: 10.13009/EUCASS2017-365

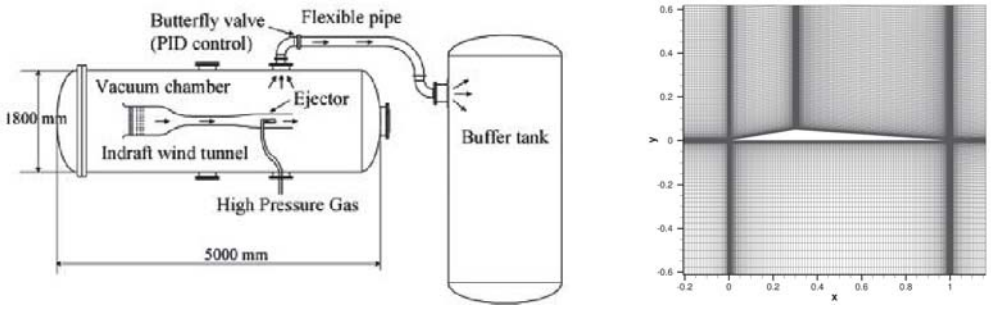

(a) Tohoku's University *Mars Wind Tunnel*

(b) Triangular airfoil's 89200 cells mesh

Figure 1: Triangular airfoil *Mars Wind Tunnel* experiment[13]

is conceivable.[3] Transition criteria, such as AHD[4] and Moore,[8] have preliminary confirmed that no transition would occur neither by amplification of Tollmien-Schlichting waves nor by separation bubble. Mesh convergence has been studied for all Navier-Stokes simulations.

3D unsteady simulations recreating the MWT test section is needed in order to recreate the same test conditions as in the experiment. Representative flow conditions ($Re_c = 3000$, $M = 0.5$) are chosen. 117000 cells 2D H-topology meshes with 242 nodes mapping the airfoil's upper surface and 151 for the lower surface have been made taking into account the test section walls with different angles of attack of the airfoil: 5°, 10° and 15°. The first cell height is set to 2.10^{-4} for chord-normalized coordinate system. From those 2D meshes, 15 millions cells 3D meshes have been constructed with 131 nodes in spanwise direction for a width of 3.3c - figure 2(a). As presented in figure 2(b), laminar

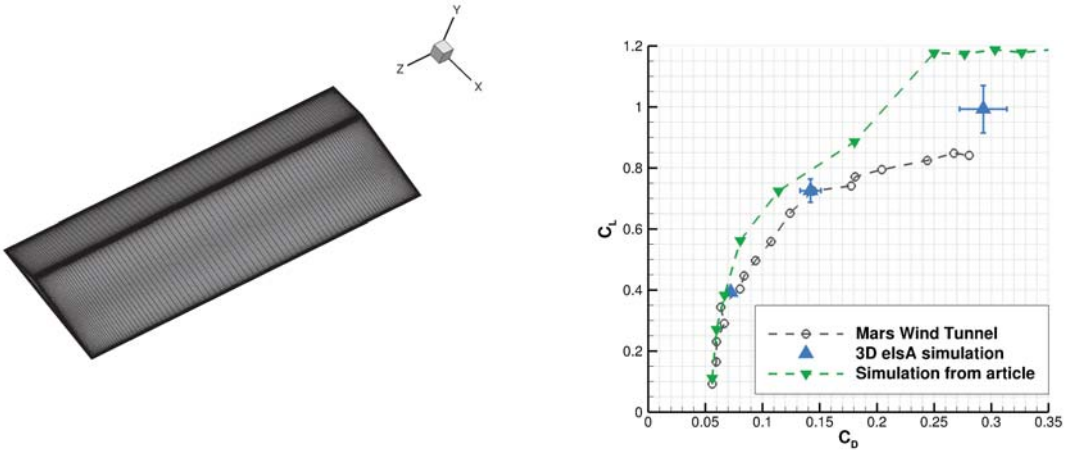

(a) Mesh mapping the 3D airfoil of 3.3c in spanwise direction recreating MWT experiment

(b) Polar comparing MWT, 3D computations from article and 3D elsA simulation with its standard deviation ($Re_c = 3000$, $M = 0.5$)

Figure 2: 3D laminar unsteady evaluations recreating the MWT experiment including the test section

unsteady Navier-Stokes solver accurately predicts the 3D forces generated at the two first angles of attack (5° and 10°). However, for the third angle of attack, corresponding to a fully detached flow, computed lift is over-estimated. Since we do not intend to evaluate highly perturbed environment, we consider the solver validated for 3D flows and by extension, we assume that it provides reliable 2D flow predictions. As presented in figure 3, computed pressure distributions show obvious side wall effect like author's PSP measurement. Direct comparison cannot be undertaken because of a lack of PSP data in the article. Since MWT experiment is not recreating a 2D flow, we use laminar elsA unsteady computations for 2D steady numerical tools assessement.

DOI: 10.13009/EUCASS2017-365

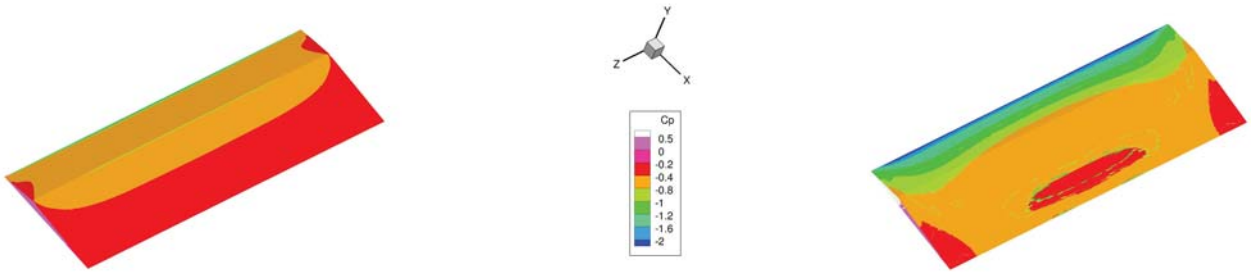

(a) C_P distributions over the airfoil at $\alpha = 5°$

(b) C_P distributions over the airfoil at $\alpha = 10°$

Figure 3: elsA computation of C_P distributions revealing a three dimensionality of the flow caused by the walls of the test section

3.3 2D steady solver assessement for airfoil optimization process

In an airfoil optimization process, a quick and effective tool is needed for performances comparison: unsteady Navier-Stokes simulations' computational cost is too significant. XFoil,[6] a potential flow solver strongly interacted with integral boundary layer formulation, provides a quick steady evaluation of lift, drag and boundary layer state. In order to evaluate laminar XFoil forces prediction, we compare it to laminar steady and unsteady elsA solver on the test case of the triangular airfoil ($Re_c = 3000$, $M = 0.5$). Mesh used for these elsA evaluations, presented on figure 1(b), counts 89200 cells with 242 nodes mapping the upper surface and 151 for the lower surface. It is noted that XFoil provides a Karman-Tsien compressibility correction for C_P and external velocity u_e. The integral boundary layer formulation is already valid for compressible flow, therefore, it may be considered as a subcritical compressible solver. As we observe in figure 4(a), taking into account unsteadiness in 2D compressible ultra-low Reynolds number

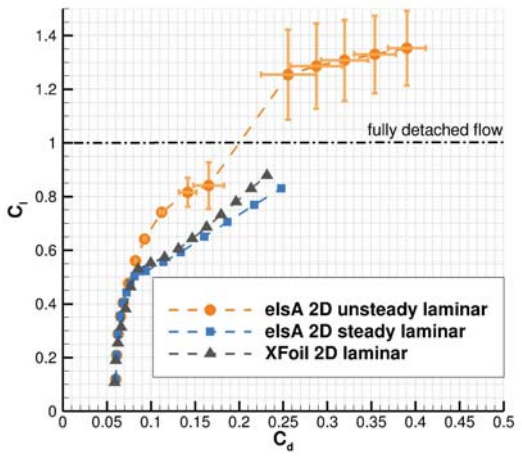

(a) Polar comparing elsA steady and unsteady 2D simulations (with standard deviation) and XFoil ($Re_c = 3000$, $M = 0.5$)

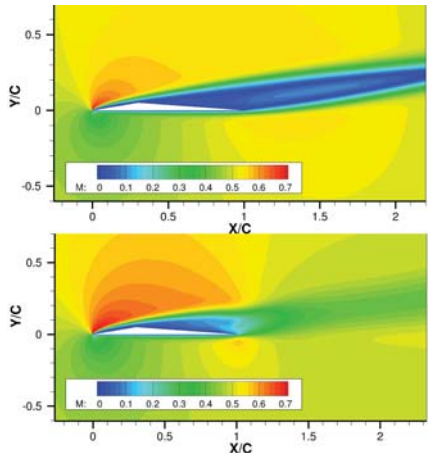

(b) Mach fields in steady case (upper) and averaged unsteady (lower) ($Re_c = 3000$, $M = 0.5$, $\alpha = 9°$)

Figure 4: Comparison of different 2D solvers on compressible ultra-low Reynolds number flows

simulations increases the forces generated by the airfoil. This is due to the recirculation zone created by boundary layer separation. For $C_l < 1$, detachment is triggered by 0.3c upper surface discontinuity - figure 4(b). For $C_l > 1$, flow is fully detached from leading to trailing edge creating a lift and drag overshoot going along with strong unsteadiness. In steady computations using XFoil and elsA, boundary layer separation creates a massive drag rise without significant lift gain causing poor aerodynamic performances. However, forces predictions anterior to heavy boundary layer separation provide valuable hint on airfoil's performances. Therefore, we consider that we can use the steady solver XFoil for airfoil comparison in an optimization process acknowledging that it does not take on board the entire physic of the flow.

DOI: 10.13009/EUCASS2017-365

4. Airfoil optimization process based on XFoil's performances evaluations

XFoil is chosen for airfoil evaluation in the optimization process because it provides quick polar generations and valuable hints on airfoil's performances. The major issue raised by XFoil is convergence: many phenomenon can cause a non-convergence. Convergence rate can be slightly enhanced but the optimization process is compeled to be extremely robust to non-convergence.

4.1 Convergence enhancement on XFoil

XFoil raises convergence issues impacting the optimization process. Its convergence rate can be enhanced by adjusting airfoil paneling parameters. First step is to properly discretize the airfoil loaded in the software, especially for leading and trailing edges. Then, different paneling parameters can be set in order to tighten panel discretization in some identified regions. It has been chosen to loop on different paneling parameters in order to reach a maximal convergence rate without an important raise in computational cost.

4.2 CST airfoil parametrization

In an optimization process, automatic airfoil generation with finite parameters is primordial. CST method[10] has been chosen because of its ability to recreate any C^2 continuous airfoil shapes with a restricted number of parameters. CST function is a 2D curve formed as the product of a class function, depicting the leading and trailing edge shape with two parameters, and a shape function, depicting the airfoil's general shape. The shape function is a linear combination of elementary Bernstein functions. Bernstein polynomials degree sets the number of parameters representing the shape function, hence its possible complexity. In this study, we used five (2+3) parameters to reflect the shape of one curve: camber or thickness distribution. Note that discontinuous airfoils, for example corrugated airfoils, cannot be represented with this parametrization method. However, XFoil is not able to simulate a recirculation zone in a corrugation.

4.3 Robust optimization method to non-convergence

From the airfoil parametrization, a set is composed of five parameters representing the camber line and/or five parameters representing the thickness distribution with CST representation. The robust method to non-convergence consists of evaluating the entire parameters domain with an increasing proximity between the different sets of parameters. As presented in figure 5(b), from each input generation N, ten sets of parameters are selected as the most effective airfoils and form a zone in the domain. The sets of parameters outside of the zone created by the ten selected are eliminated from the optimization domain: a new domain is formed and a new input generation $N+1$ is evaluated. The process is robust to non-convergence because it does not learn from previous evaluations: we observe an unconverged set of parameters from generation N represented with a green triangle. Since its set of parameters is part of the zone formed by the most effective airfoils of its generation, it is still part of the new generation domain and a close set of parameters is going to be evaluated and converged. However, sufficient proximity on the domain is needed in order to avoid the elimination of unconverged effective sets of parameters: it demands a very important number of sets. Each generation counts at least 50 000 sets of parameters. The optimization process relies on its selection process and more precisely on its performance function - figure 5(a). Since Martian atmosphere is highly turbulent, the blade's flight conditions can fluctuate. Hence, performance function needs to be averaged on an important range of incidence and Reynolds number for building an effective airfoil not only for competitiveness in specific flight conditions[7] but in the entire hover range of a Martian micro air vehicle. Each set of parameters, representing an airfoil shape, is evaluated on three Reynolds numbers representative of the entire Martian MAV flight domain: $Re_c \in [2000,\ 6000,\ 10\,000]$. For each Reynolds number, a temporary performance function is built as the mean value between lift-to-drag ratio and endurance coefficient:

$$P1(\alpha) = \frac{1}{2}\left[\frac{C_l^{3/2}}{C_d} + \frac{C_l}{C_d}\right] \tag{1}$$

From temporary function $P1$, the optimal angle of attack is determined: $\alpha_{opt} = \max_\alpha P1(\alpha)$.
A new temporary performance function is defined on a range of angles of attack surrounding the optimal α_{opt}:

$$P2(Re_c) = \frac{1}{5} \sum_{\alpha \in [\alpha_{opt},\ \alpha_{opt}\pm 1^\circ,\ \alpha_{opt}\pm 2^\circ]} P1(\alpha) \tag{2}$$

DOI: 10.13009/EUCASS2017-365

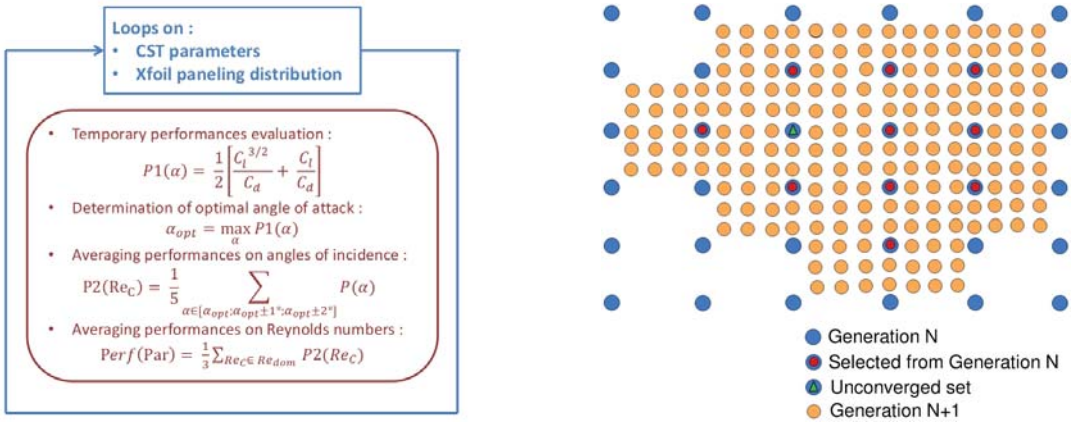

(a) Summary of the optimization process

(b) 2D representation of the selection process

Figure 5: Robust optimization process providing the best set of parameters for a robust airfoil

Finally, the performance function corresponding to a set of parameters $Perf(Par)$ is defined as the mean value between the $P2$ functions on the Reynolds number range.

$$Perf(Par) = \frac{1}{3}\sum_{Re_c\in[2000,\ 6000,\ 10\ 000]} P2(Re_c) \tag{3}$$

The purpose of the optimization process is to generate an airfoil maximizing this performance function. For each generation, a shape convergence matrix β based on the selected sets of parameters S is formed for final convergence determination.

$$\forall(n,p)\in[\![1,10]\!] \qquad \beta(n,p) = \frac{\|S(n) - S(p)\|_{L^2}}{\|S(n)\|_{L^2}} \tag{4}$$

with $S(n)$ and $S(p)$ being two selected sets of parameters.
The optimization process is considered converged if: $\max(\beta) < 10\%$. This convergence criterion permits verification of shape proximity between the ten selected airfoil. Speed and parallelization of performance evaluations are essentials to this method. A single generation counts at least 50 000 sets of parameters evaluated several times, if not directly converged with the default paneling parameters, for each of the three Reynolds numbers. Approximately half a million XFoil evaluations are carried out in each generation.

5. Results of compressible and incompressible airfoil optimization for ultra-low Reynolds number flows

We acknowledge that heavy boundary layer separations are causing poor aerodynamic performances or non-convergence in XFoil, hence, airfoils enhancing vortex production cannot be truly evaluated and the optimization process aims at generating airfoils shifting the boundary layer separation downstream. For flow behavior apprehension, optimization has been carried out step by step, adding gradual complexity. First in incompressible flows: camber line optimization with a prescribed thickness distribution, then thickness distribution optimization and, since they are co-dependent, optimization of both. Finally, the impact of compressible flows is assessed with an optimization of both camber line and thickness distribution.

5.1 Incompressible camber line optimization with prescribed thickness distribution

The prescribed thickness distribution is a 2% relative thickness with round leading edge and sharp trailing edge: it has been studied on a sample of hundred camber lines for enhancing XFoil's convergence rate. Figure 6(a) provides the absolute optimum camber line based on the performance function on the entire Reynolds number range, c.f. equation (3). In addition, the last generation's domain optimum for each Reynolds number is displayed indicatively for optimization process validation and physics comprehension. Note that the optimal airfoils for $Re_c = 6000$ and $Re_c = 10\,000$ are the same. General shape of each optimal camber line follows the same pattern: a cambered leading edge for proper flow adaptation avoiding early boundary layer separation. A slightly tilted flat middle shape permitting to delay boundary

DOI: 10.13009/EUCASS2017-365

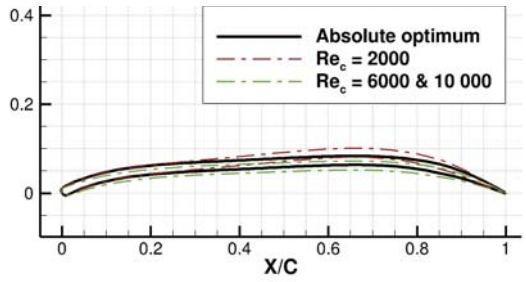

(a) Optimum airfoil shapes of the last camber line optimization generation

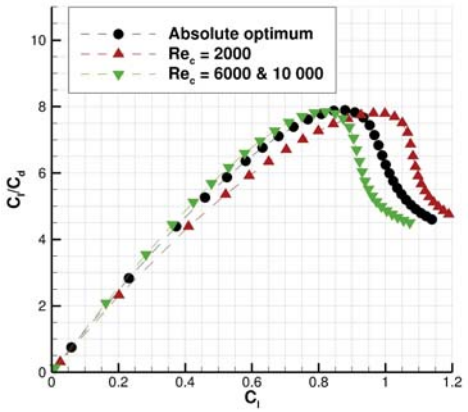

(b) XFoil's polar in flight conditions ($Re_c = 2000$, $M = 0.1$)

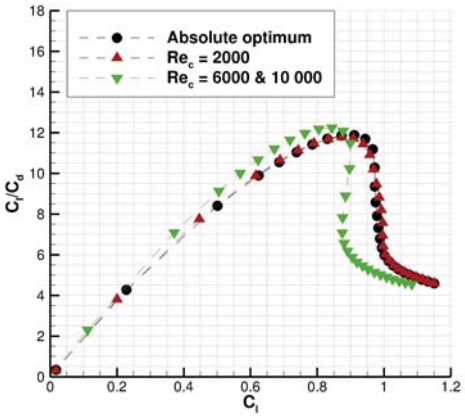

(c) XFoil's polar in flight conditions ($Re_c = 6000$, $M = 0.1$)

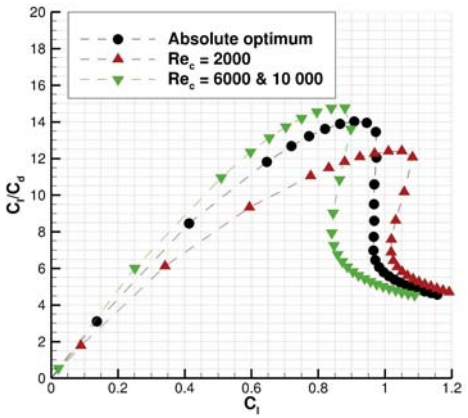

(d) XFoil's polar in flight conditions ($Re_c = 10\ 000$, $M = 0.1$)

Figure 6: Optimization's last generation optimum camber line shapes for the different Reynolds numbers and the Reynolds number range: $Re_c \in [2000,\ 6000,\ 10\ 000]$

layer detachment. And the highly cambered trailing edge fixes the separation point. Hence, optimal airfoils are producing sufficient lift with high camber while shifting the boundary layer separation downstream. Two incompressible camber line optimizations from literature provide the same general optimal camber line shape for Reynolds number $Re_c = 6000$[11] and $Re_c \in [6000, 16000]$.[12]

As for the performances, we observe in figure 6(b) that the highly cambered optimum for $Re_c = 2000$ provides a later drag rise permitting wider range of C_l having good lift-to-drag ratio for flight conditions ($Re_c = 2000$, $M = 0.1$). For larger Reynolds numbers - figure 6(c.d) - boundary layer thickening no longer compensates the adverse pressure gradient and boundary layer separation implies high drag production. Hence, its camber is too important for $Re_c > 6000$. The absolute optimum produces lift without triggering an important drag increase for any $Re_c \in Re_{dom}$: the optimization process produces airfoils having proper lift-to-drag ratio over a wide range of lift on the entire Reynolds number range.

5.2 Incompressible thickness distribution optimization from absolute optimal camber line

From the absolute optimal camber line, a minimum relative thickness constraint is defined in order to avoid unfeasible airfoils regarding manufacturing process. For constraint's magnitude evaluation, several optimizations have been carried out with different values of the constraint: $T_{min} \in [1\%,\ 2\%,\ 3\%]$. As presented in figure 7(a), for each T_{min} constraint, the optimization process tends to a specific thickness distribution: important camber line gradient, at $X/C = 0.15$ & 0.8, implies the lowest thickness (T_{min}). Highest thickness is reached in the middle of the airfoil and at round trailing edge. Optimized thickness distribution gives the impression of smoothing adverse pressure gradient in order to avoid boundary layer separation - figure 8(a). Therefore, camber line and thickness distribution are probably

DOI: 10.13009/EUCASS2017-365

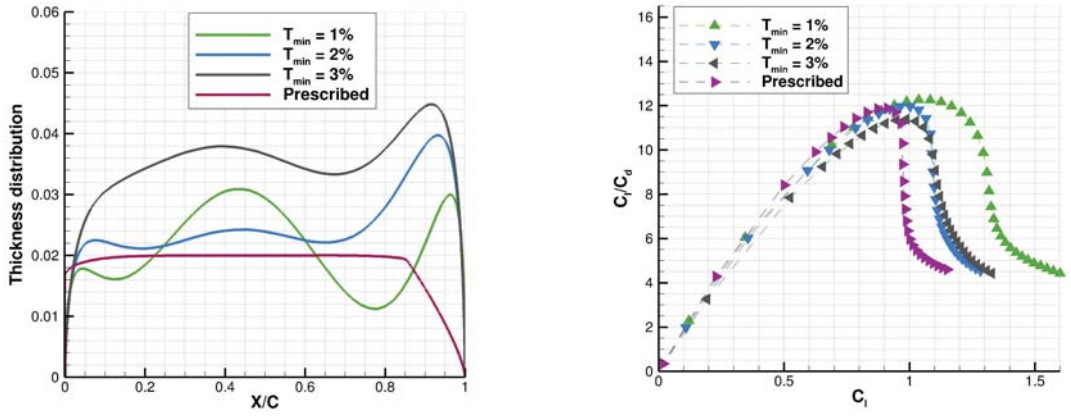

(a) Optimal thickness distributions for different T_{min} constraints compared to the prescribed: enhancing XFoil's convergence rate

(b) XFoil's polar in flight conditions ($Re_c = 6000$, $M = 0.1$) for different thickness distributions

Figure 7: Impact of the minimum relative thickness constraint T_{min} on optimized thickness distribution and aerodynamic performances

correlated: a general airfoil shape optimization is needed.
As for the aerodynamic performances, $T_{min} = 1\%$ is the most effective constraint providing satisfactory lift without massive drag generation - figure 7(b).

5.3 Incompressible general airfoil shape optimization: camber line and thickness distribution

The two CST-represented lines are optimized simultaneously. With ten variables, much more generations are needed and the optimization process is greater in terms of computational time and number of tested airfoils. The minimum relative thickness constraint is set to $T_{min} = 1\%$. As presented in figure 8(a), general airfoil optimization provides a less cambered airfoil than the optimized camber line with a prescribed thickness distribution. Moreover, it presents the same leading and trailing edges thickness distribution as the optimized thickness distribution from a prescribed camber line. Yet, the thinner parts at $X/C = 0.15$ & 0.8 are no longer present, proof that thickness distribution optimization was compensating for the over-cambered line designed for the prescribed leading edge and trailing edge distributions. It is noticed that, unlike initial guess, the optimization process is converging toward an approximately 2% relative thickness distribution with a minimal relative thickness constraint of $T_{min} = 1\%$.
Figure 8(b.c) exhibit a better lift-to-drag ratio on a wider range of coefficient of lift at each optimization complexity increment. This is due to better leading edge flow adaptation and trailing edge decompression permitting wider pressure distributions - figure 8(d).

5.4 Compressible general airfoil shape optimization: camber line and thickness distribution

The final step consists of assessing the impact of compressibility in the general airfoil shape optimization. We remind that XFoil may be considered as a compressible solver for subsonic flows: flow rate is set to $M = 0.5$ for avoiding local shocks appearance. As in the incompressible case, minimum relative thickness constraint is set to $T_{min} = 1\%$. As presented in figure 9, compressible airfoil optimization results in an equivalent thickness distribution with a reduced camber compared to incompressible optimization. In compressible flows, boundary layer separation is more easily triggered: the reduced camber permits to delay high drag production at higher lift, hence, a better lift-to-drag ratio is achieved. We note that in both cases lift-to-drag ratio drops quickly after reaching its maximal value: for robustness, design C_l in rotor generation has to be weakened.

DOI: 10.13009/EUCASS2017-365

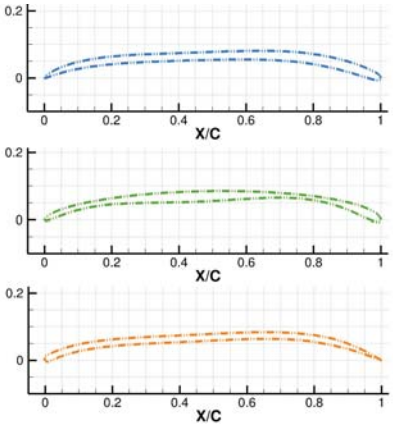

(a) Incompressible XFoil optimal airfoil shapes with a predefined thickness distribution (lower), a pre-optimized camber line (middle) and general shape optimization (upper)

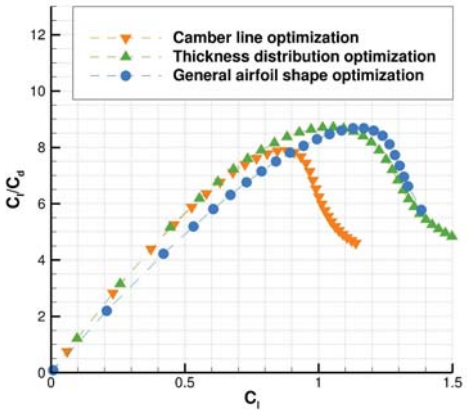

(b) XFoil's lift-to-drag ratio in flight conditions ($Re_c = 2000$, $M = 0.1$)

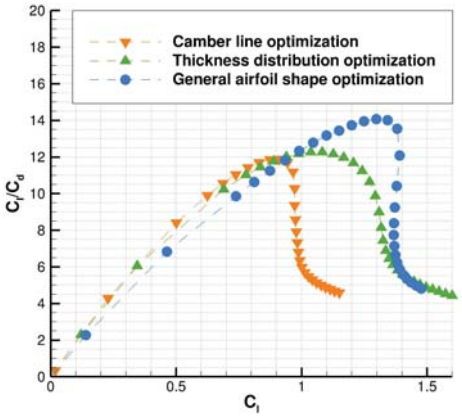

(c) XFoil's lift-to-drag ratio in flight conditions ($Re_c = 6000$, $M = 0.1$)

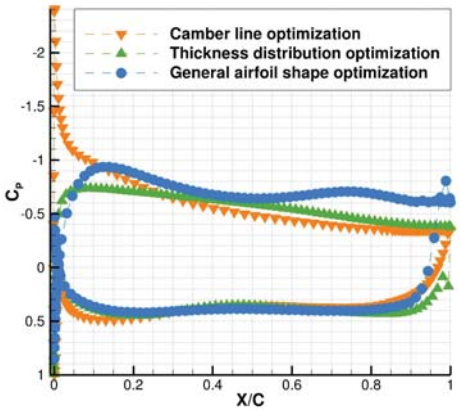

(d) XFoil's pressure coefficient for $C_l \sim 0.94$ in flight conditions ($Re_c = 6000$, $M = 0.1$)

Figure 8: Incompressible general airfoil optimization performances comparison with the different optimization steps

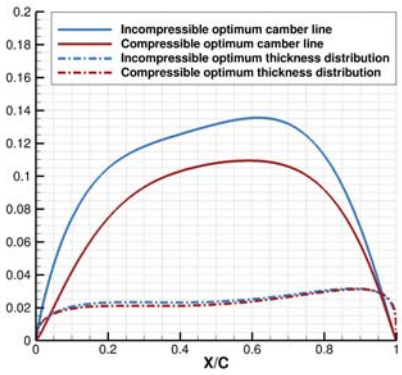

(a) General airfoil shape comparison for a compressible and incompressible optimization

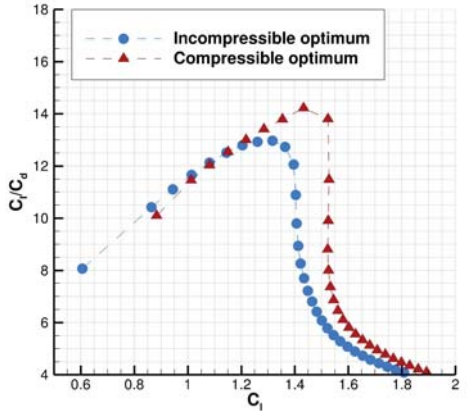

(b) XFoil's polar in flight conditions ($Re_c = 6000$, $M = 0.5$)

Figure 9: Compressible general airfoil optimization XFoil's performances comparison with incompressible optimum

DOI: 10.13009/EUCASS2017-365

6. Evaluation of the optimized airfoils in 2D unsteady compressible Navier-Stokes simulations compared to airfoils picked from literature

Since the optimization process is based on a simplified steady solver performances evaluations, it is essential to numerically audit the optimal airfoils with a validated solver. ONERA's unsteady solver elsA has been validated on 3D compressible ultra-Low Reynolds number flows and meshes are based on the same cells density as for the triangular airfoil - part 3.

6.1 Assessment of the optimized airfoils for different Reynolds numbers in compressible flows

Figure 12 exhibits the aerodynamic performances of each optimization steps' optimal airfoil in compressible ultra low Reynolds number flows. They have very close unsteady Navier-Stokes performance polars and tendencies are the

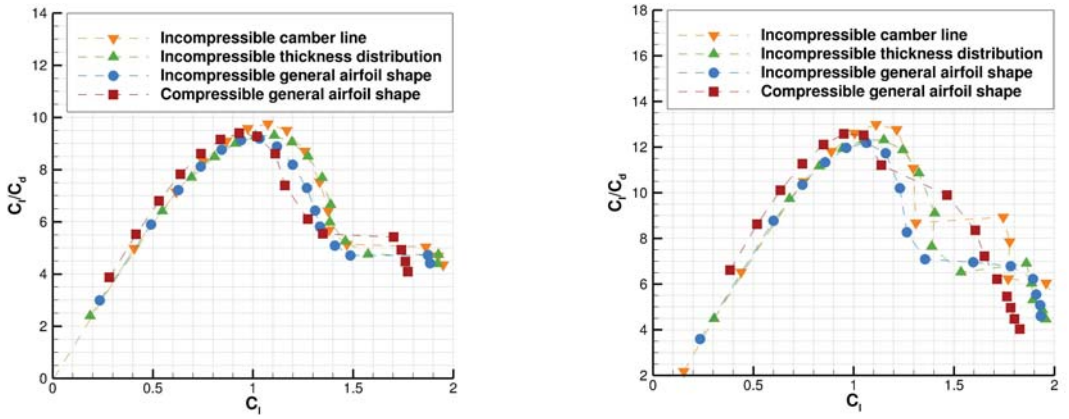

(a) Averaged unsteady N-S polar in flight conditions ($Re_c = 3000$, $M = 0.5$)

(b) Averaged unsteady N-S polar in flight conditions ($Re_c = 6000$, $M = 0.5$)

Figure 10: 2D aerodynamic performances of the optimized airfoils evaluated with elsA

same for each Reynolds number. Compressible optimum generates lower drag for $C_l < 1$ than more highly cambered optimized airfoils. However, the most highly cambered airfoils suffer the drag rise at higher lift generation. Therefore, the 2D optimal camber line depends on the aimed range of lift coefficient. We also note that the incompressible camber line optimization provides the best lift-to-drag ratio for $Re_c \in [3000, 6000]$. It means that thickness distribution optimization for a given camber line did not enhance 2D unsteady aerodynamic performances.

6.2 Impact of round trailing edge on aerodynamic performances

The main difference between the optimized and the prescribed thickness distribution comes from trailing edge definition, therefore, we intend to evaluate the impact of this difference by producing an optimal compressible airfoil with a sharp trailing edge replacing its unusual round shape - figure 11(a). As presented in figure 11(b-c), sharp trailing edge allows a slight drag and unsteadiness reduction compared to round trailing edge. However, gap in 2D aerodynamic performances for different trailing edge thickness distributions is minor. Considering the Reynolds number range, boundary layer growth and the recirculation zone triggered by separation at upper surface minimize the magnitude of trailing edge shape. Therefore, the difference in performances between the incompressible camber line and the incompressible thickness distribution comes from leading and trailing edge definition. We note that with steady and unsteady 2D simulation, unsteadiness rise is highly correlated with drag rise for each optimized airfoil. However, since they were optimized for shifting the boundary layer separation downstream, a comparison with airfoils enhancing vortex production is required.

6.3 Compressible and incompressible evaluation of a steady optimized airfoil compared to airfoils picked from literature

The steady optimization process based on XFoil is evaluated with a comparison to airfoils picked from literature. We consider as our optimized airfoil the compressible general airfoil shape since we are interested in low drag production.

DOI: 10.13009/EUCASS2017-365

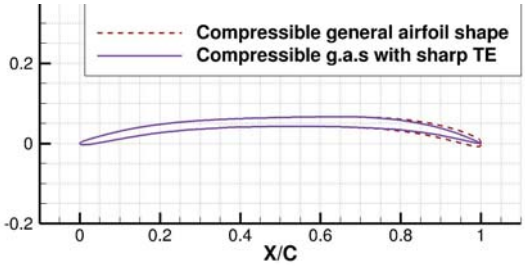

(a) Modification of trailing edge thickness distribution: from round to sharp

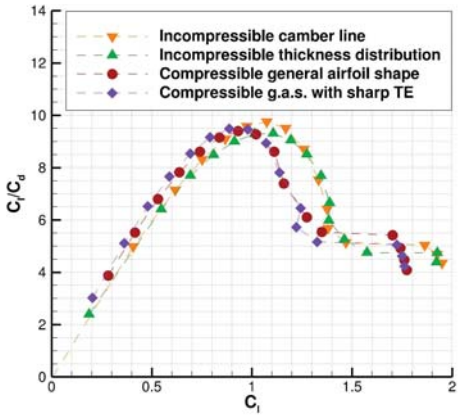

(b) Averaged unsteady N-S polar in flight conditions ($Re_c = 3000$, $M = 0.5$)

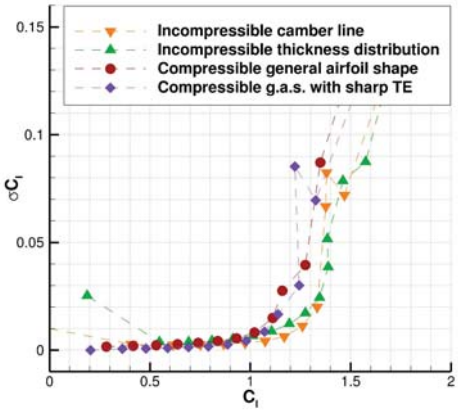

(c) Standard deviation in lift coefficient for flight conditions ($Re_c = 3000$, $M = 0.5$)

Figure 11: Evaluation of the impact of round trailing edge on aerodynamic performances and unsteadiness production

In addition to the previously evaluated triangular airfoil - part 3.3 - two airfoils considered in the literature as effective in ultra low Reynolds number flows are computed with the validated solver. The 6% cambered plate - figure 13(b) - has been proven experimentally to be the most effective classical airfoil for martian flight conditions[14,11].[1] And since biomimicry tends to drive us toward corrugated airfoils enhancing vortex production, a dragonfly airfoil - figure 13(d) - is picked: it was also experimentally proven to be the most aerodynamically effective from three sections at different radius of a dragonfly wing at ultra-low Reynolds number.[9] Both airfoils are generated with a 2% relative thickness distribution for numerical evaluation. We observe in figure 12 that airfoils delaying boundary layer separation provide far

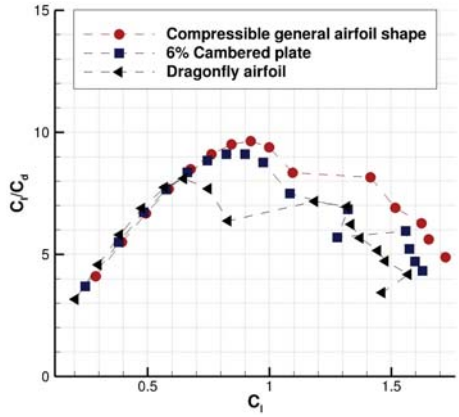

(a) Averaged unsteady N-S polar in flight conditions ($Re_c = 3000$, $M = 0.1$)

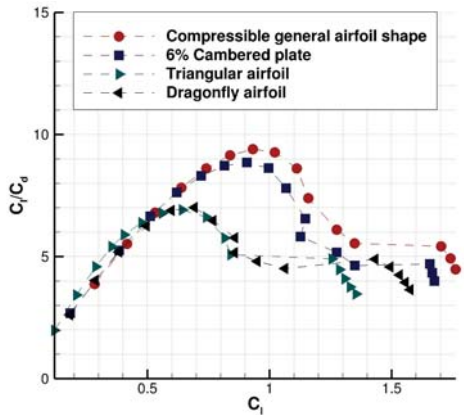

(b) Averaged unsteady N-S polar in flight conditions ($Re_c = 3000$, $M = 0.5$)

Figure 12: 2D aerodynamic performances evaluated with elsA of an optimized airfoil compared to airfoils from literature[9,11,13]

DOI: 10.13009/EUCASS2017-365

better 2D lift-to-drag ratio than the airfoils enhancing vortex production we tested. Therefore, even for airfoils enhancing vortex production, drag production is highly correlated with unsteadiness production. We note that performances are very similar in compressible and incompressible flows for low lift production. At higher lift production, drag rise is slightly lighter in incompressible flows. Figure 13 displays the averaged mach number contours for a production of

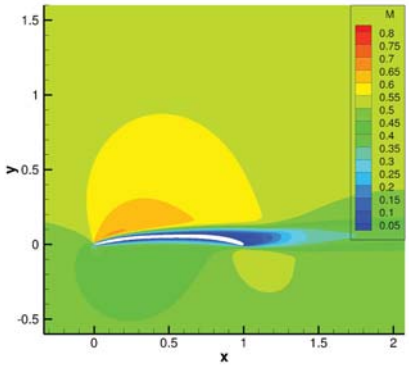

(a) Averaged unsteady N-S mach fields in flight conditions ($Re_c = 3000$, $M = 0.5$, $\alpha = 5°$) for the compressible general airfoil shape

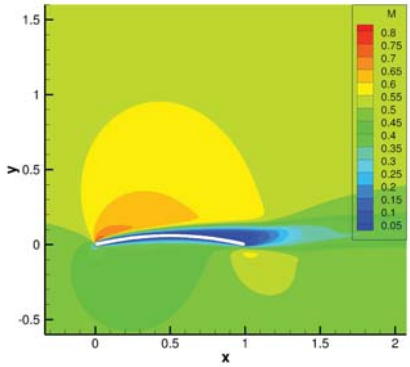

(b) Averaged unsteady N-S mach fields in flight conditions ($Re_c = 3000$, $M = 0.5$, $\alpha = 6°$) for the 6% cambered plate

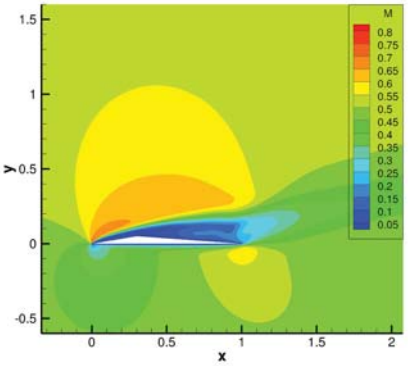

(c) Averaged unsteady N-S mach fields in flight conditions ($Re_c = 3000$, $M = 0.5$, $\alpha = 10°$) for the triangular airfoil

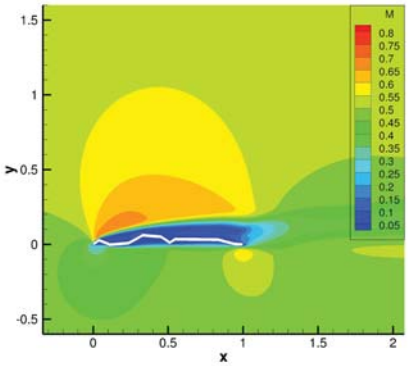

(d) Averaged unsteady N-S mach fields in flight conditions ($Re_c = 3000$, $M = 0.5$, $\alpha = 7°$) for the dragonfly airfoil

Figure 13: 2D averaged unsteady N-S mach fields evaluated with elsA

$C_l \sim 0.85$ of each airfoil in figure 12(b). It confirms that 6% cambered plate and the optimized airfoil are shifting the boundary layer separation downstream for low unsteadiness and drag production. Corrugated and triangular airfoils trigger boundary layer detachment early in chordwise direction degrading 2D performances. However, we acknowledge that only one corrugated airfoil has been computed: generalization on the entire range of airfoils enhancing vortex production would be unwise.

To conclude, XFoil provides valuable hints on airfoil performances permitting to figure out trends in airfoil shapes optimization. 2D unsteady Navier-Stokes evaluations do not show large differences in performances for airfoils postponing boundary layer separation. Nevertheless, a slight 2D performances enhancement might have a greater impact on 3D flows.

7. Rotor design process using blade-element/vortex method

In order to evaluate the impact of airfoil optimization in 3D, a automatized blade-element/vortex method rotor design process has been characterized.

Planform and twist design process is automatized based on 2D unsteady Navier-Stokes performances evaluation. Blade-element/vortex software QMIL/QPROP tends to generate low number of blades and large chords especially at blade's root for low power loading (thrust divided by power) production and low rotational speed for a given mass to sustain. However, important chords and/or number of blades may cause heavy blade-to-blade interactions: this phenomenon is not taken into account in the blade-element/vortex method. Therefore, we set number of blades to three,

DOI: 10.13009/EUCASS2017-365

lift to 100 g (0.37N) and maximum chord at 6 cm radius to 6 cm ($c = R$): a spline permits root chord distribution closing without chord overshoot while pitch angle remains constant. The design method's main objective is to generate the chord distribution lifting 100 g at the lowest rotational speed possible. Furthermore, regarding manufacture issues, a minimum absolute thickness is set to 0.5 mm. New thickness distribution optimizations have been carried out with a minimum relative thickness set to 10% and 20% from the camber lines of each evaluated airfoils. Tip airfoil shape and performances have been interpolated between the optimal thickness distribution and the thicker airfoils in order to respect the absolute thickness constraint. In QPROP, 2D lift and drag formulations are represented by the following variables:

$$Cl(\alpha) = (Cl_0 + Cl_a\alpha)/\beta \tag{5}$$

$$Cd(Cl, Re_c) = \left[Cd_0 + Cd_2 * (Cl - ClCd_0)^2\right] * \left[Re_c/Re_{ref}\right]^{Re_{exp}} \tag{6}$$

where $Re_{ref} = 3000$ in our case and β represents the compressibility correction. Prandlt-Glauert and Karman-Tsien have been compared to elsA's 2D laminar unsteady N-S compressibility evaluation: Karman-Tsien provides a closer compressibility correction. Therefore, it has been changed manually in the software. Other variables are evaluated with a linear and a non-linear regression based on 2D unsteady Navier-Stokes performances at flight conditions ($Re_c = 3000$, $M = 0.1$). Re_{exp} is evaluated for best fitting value with several XFoil evaluations at different Reynolds number $Re_c \in [500, 1000, 2000, 3000, 5000, 7000, 9000, 12000]$.

Rotor manufacturing for the upcoming experimental campaign is provided by a 3D liquid resin printer (Formlabs - Form 2). This tool allows a fast ($\sim$ 10h per rotor), accurate and inexpensive rotor production. Since chords are significant compared to a classical helicopter, airfoils sections are projected onto concentric circles for better match between simulation and reality, as in marine BEMT. The optimized planform distribution for the compressible general airfoil shape optimum is presented in figure 14(a).

For evaluating the influence of design constraints on rotor performances: two different types of rotor have been generated. First is a 5 bladed rotor - 14(b) - and second has a looser chord restriction - 14(c). Both rotors introduce a chord restriction preventing from blade overlapping. We acknowledge that aerodynamic comparison from blade-

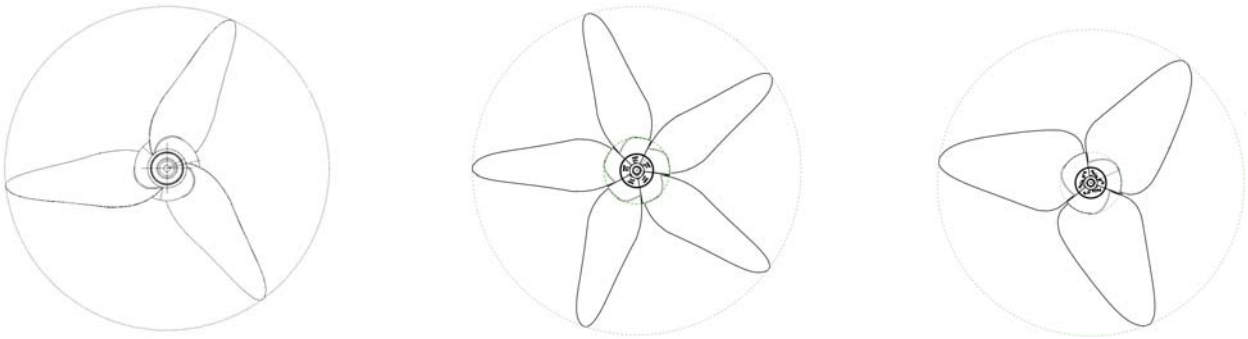

(a) 3 bladed rotor generated by design process with chord restriction

(b) 5 bladed rotor generated by design process preventing from blade overlapping

(c) 3 bladed rotor generated by design process preventing from blade overlapping

Figure 14: with compressible general airfoil shape

element/vortex method evaluations is not relevant since it does not take into account blade-to-blade interaction nor 3D flows effects. But, tendencies show a better power loading in cases of low number of blades and important chords.

8. Experimental facility recreating Martian atmospheric conditions

The rotor design process being based on 2D unsteady computations, 3D tendencies will be evaluated with an upcoming experimental campaign. The experimental campaign's purpose is to recreate the Martian flight conditions for rotor evaluation and comparison. The facility is a 18 m^3 tank located at ONERA's Fauga center. Inside the tank, an ISAE-SUPAERO testbed is incorporated in order to measure thrust and torque generated by rotors - figure 15. Note that rotor wake heads toward tank's tube, significantly reducing flow recirculation. Cameras are disposed inside and outside the tank in order to evaluate unsteady behaviors of the different rotors. Two phases are planned for evaluating the impact of gaz composition on aerodynamic performances: first in air and second with 96% of CO_2 in the tank, recreating Martian atmospheric carbon dioxide percentage. Since tank temperature differs from Martian atmospheric temperature, in both cases aimed pressure has been calculated in order to recreate Martian kinematic viscosity, therefore to recreate Martian flight Reynolds number.

DOI: 10.13009/EUCASS2017-365

(a) ISAE-SUPAERO's experimental testbed in the depressurised tank

(b) 18 m^3 depressurized tank located at ONERA's Fauga center

Figure 15: Experimental device evaluating rotors in Martian atmosphere

9. Conclusion

The main conclusions drawn on compressible ultra low Reynolds number flows during this study are the following:
• Laminar unsteady Navier-Stokes solver elsA permits a proper flow simulation and forces predictions in an undisturbed 3D environment.
• 2D steady computations allow to assess the incidence of boundary layer separation and to provide valuable hints on airfoil performances. Making them useful tools for airfoil optimization.
• Effective airfoils for 2D ultra low Reynolds number flows are highly cambered airfoils with leading edge and trailing edge camber allowing to delay boundary layer separation and unsteadiness production. Acknowledging that we only computed two airfoil enhancing vortex production including one corrugated airfoil.[9]
• Subcritical compressibility has little impact on 2D aerodynamic performances but eases boundary layer detachment. Therefore, a compressible airfoil optimization tends to a less cambered airfoil than incompressible airfoil optimization. Future work will include the evaluation of airfoil shape's impact on 3D rotor aerodynamic performances. The upcoming experimental campaign will provide aerodynamic performances and 3D unsteady rotor Navier-Stokes computations will provide the flow behavior comprehension.

References

[1] F. Bohorquez. *Rotor Hover Performance and System Design of an Efficient Coaxial Rotary Wing Micro Air Vehicle*. PhD thesis, University of Maryland, 2007.

[2] L. Cambier, M. Gazaix, S. Heib, S. Plot, M. Poinot, J.P. Veuillot, J.F. Boussuge, and M. Montagnac. An overview of the multi-purpose elsa flow solver. *Journal Aerospace Lab*, 2011.

[3] B.H. Carmicheal. Low reynolds number airfoil survey. *NASA CR 165803*, 1981.

[4] J. Cliquet. *Calcul de la transition laminaire-turbulent dans les codes Navier-Stokes. Application aux géométries complexes*. PhD thesis, Institut Supérieur de l'Aéronautique et de l'Espace, 2007.

[5] R. W. Derksen, M. Agelinchaab, and M. Tachie. Characteristics of the flow over a naca 0012 airfoil at low reynolds numbers. *WIT Transactions on Engineering Sciences*, 2008.

[6] M. Drela. Xfoil: an analysis and design system for low reynolds number airfoils. In *Conference on Low Reynolds Number Airfoil Aerodynamics*, 1989.

[7] M. Drela. Pros ans cons of airfoil optimization. *Frontiers of Computational Fluis Dynamics*, 1998.

[8] C. Gazley. Boundary-layer stability and transition in subsonic and supersonic flow. *Journal of the Aeronautical Sciences*, 1952.

DOI: 10.13009/EUCASS2017-365

[9] A. Kesel. Aerodynamic characteristics of dragonfly wing sections compared with technical aerofoils. *The Journal of Experimental Biology*, 2000.

[10] B.M. Kulfan and J.E. Bussoletti. "fundamental" parametric geometry representations for aircraft component shapes. In *11th AIAA/ISSMO Multidisciplinary Analysis and Optimization*, 2006.

[11] P.J. Kunz. *Aerodynamics and Design for Ultra-Low Reynolds number flight*. PhD thesis, University of Stanford, 2003.

[12] Z. Liu, L. Dong, J.M. Moschetta, J. Zhao, and G. Yan. Optimization of nano-rotor blade airfoil using controlled elitist nsga-ii. *International Journal of Micro Air Vehicles*, 2014.

[13] P.M. Munday, K. Taira, T. Suwa, D. Numata, and K. Asai. Nonlinear lift on a triangular airfoil in low-reynolds-number compressible flow. *Journal of Aircraft*, May-June 2015.

[14] H. Nagai, K. Asai, D. Numata, and T. Suwa. Characteristics of low-reynolds number airfoils in a mars wind tunnel. In *51th AIAA Aerospace Sciences Meeting*, 2013.

[15] R. Shrestha, M. Benedict, V. Hrishikeshavan, and I. Chopra. Hover performance of a small-scale helicopter rotor for flying on mars. *Journal of Aircraft*, 2016.

[16] S. Sunada, T. Yasuda, and K. Yasuda ans K. Kawachi. Comparison of wing characteristics at an ultralow reynolds number. *Journal of Aircraft*, 2002.

[17] T. Tsuchiya, D. Numata, T. Suwa, and K. Asai. Influence of turbulence intensity on aerodynamic characteristics of an naca 0012 at low reynolds numbers. In *51st AIAA Aerospace Sciences Meeting*, 2013.

[18] S. Wang, Y. Zhou, and Md. Alam. Effects of reynolds number and turbulent intensity on a low reynolds number airfoil. *AIAA Aviation*, 2014.